PAPER

Five-fold twinned copper nanowire gas diffusion electrodes for electrochemical CO_2 reduction with enhanced C_2 product selectivity and stability

Hsin-Yu Chen, [ID] [ab] Bhavin Siritanaratkul, [ID] [a] Chien-Neng Liao [ID] *[bc] and Alexander J. Cowan [ID] *[a]

Copper nanowires with fivefold twinned structures (t-CuNWs) are shown to be effective as cathode catalysts for the electrochemical CO_2 reduction reaction (CO_2RR) in a zero-gap electrolyzer to produce ethylene. The t-CuNWs, with surfaces enclosed by (100) facets, were selected for their enhanced CO adsorption strength, which along with the presence of the twin boundary defects, are proposed to promote C–C coupling—a key pathway toward multi-carbon (C_2) products. We also find that the entangled t-CuNWs exhibit enhanced hydrophobicity when compared to commercial Cu nanoparticles (CuNPs), which reduces electrode flooding and contributes to enhance the stability of the cathode. These characteristics distinguish t-CuNWs from CuNPs in terms of activity (overpotential, selectivity) and stability. The t-CuNWs exhibited ~40% C_2H_4 Faradaic efficiency (FE) for more than 4 hours under a current density of 100 mA cm^{-2}, while commercial CuNPs exhibited ~20% C_2H_4 FE for less than 4 hours and the CuNPs devices consistently required increased operating voltages. These findings highlight the potential of (100) faceted t-CuNWs for C_2 product formation in CO_2RR with facet engineering and hydrophobicity control.

Introduction

According to the report by the International Energy Agency, global energy-related CO_2 emissions increased by 1.1% in 2023, rising by 410 million tonnes compared to 2022, reaching a record high of 37.4 billion tonnes.[1] The electrochemical reduction of carbon dioxide (CO_2RR) has emerged as a promising pathway to produce value-added chemicals and fuels from waste CO_2 emissions, providing a way to achieve carbon neutral chemical feedstocks. There is particular interest in the CO_2RR into multi-carbon (C_2) products such as ethylene (C_2H_4), ethanol, and acetate, with C_2H_4 being noted to have both a suitably high market price, and level of demand, to make it a suitable product to target from CO_2RR.[2] However, fundamental challenges, including low selectivity for C_2 products, the limited stability of catalysts and devices, and low energy efficiencies at industrially relevant conditions, exist. Techno-economic analyses (TEAs) for industrial-scale CO_2RR for various products, including carbon monoxide, formic acid and C_2H_4 production show that C_2H_4 production require either

decreases in electricity costs,[3] or reductions in the operating voltage and Faradaic efficiency (FE) for C_2H_4 production to be commercially viable.[4]

For C_2 production, Cu stands out as the most promising metal, being capable of facilitating C–C coupling, a crucial step toward the formation of C_2 products because of its moderate CO binding strength and weak H adsorption strength, which suppresses the competing hydrogen evolution reaction (HER).[5–9] Notably, the Cu(100) facet has been identified as having the highest selectivity towards C_2H_4 formation, whereas Cu(111) preferentially yields methane (CH_4), a lower-value product.[10–12] Cu(110) is also reported to generate high-value multi-carbon products, but a broader product distribution increases separation costs.[11,13] Among the low index facets, Cu(100) is therefore the most attractive choice for C_2H_4 production. Beyond facet engineering, studies have revealed that structural defects such as grain boundaries, steps, and kinks also play critical roles in enhancing CO_2RR activity and selectivity. These low-coordinated sites provide favorable environments promoting the C–C coupling process. For instance, Cu with surface steps was proven to enhance the C_2 product selectivity and prevent HER by facilitating C–C coupling at undercoordinated active sites.[14] Furthermore, *operando* 4D-STEM investigations have revealed that Cu surfaces dynamically reconstruct under reaction conditions, forming grain boundaries and undercoordinated sites that act as active sites for *CO adsorption and activation.[15] Recent studies have

a *Department of Chemistry and Stephenson Institute for Renewable Energy, University of Liverpool, Liverpool L69 7ZF, UK. E-mail: a.j.cowan@liverpool.ac.uk*

b *Department of Materials Science and Engineering, National Tsing Hua University, Hsinchu 300044, Taiwan. E-mail: cnliao@mx.nthu.edu.tw*

c *College of Semiconductor Research, National Tsing Hua University, Hsinchu 300044, Taiwan*

revealed that catalyst morphology dynamically evolves significantly from its pristine structure under CO_2RR as proved by *operando* liquid-cell STEM. This evolution can involve the formation of new grain boundaries, restructuring of surface facets, and localized dissolution–redeposition processes. These morphological changes not only influence the electrochemical stability but also affect product selectivity.[16] These findings suggest that defect engineering, including twin boundaries, offers a powerful strategy to steer product selectivity toward high-value C_2 species in CO_2RR.

In addition to catalyst facet engineering, the structural design of the Cu catalyst on the electrode also plays a crucial role in optimizing performance, particularly under the practical scenario using gas diffusion electrodes (GDE) at high current density. Conventional Cu-based catalysts, such as Cu nanoparticles (CuNPs), often suffer from poor selectivity and stability under these conditions, primarily attributed to GDE flooding and bicarbonate formation during long-term operation.[17–20] To mitigate flooding and bicarbonate formation in GDE, a high aspect-ratio structure such as nanowires is desirable because it leads to smaller pores in the catalyst layer, which increases capillary pressure and subsequently hydrophobicity.[21,22] A recent review also showed the potential application of 1D nanowire structure to the CO_2RR field to enhance the activity, selectivity, and stability.[23]

Considering these factors, five-fold twinned Cu nanowires (t-CuNWs) serve as a target catalyst morphology. Note that the twinned structure is a two-dimensional defect where two regions of a crystal share a mirror symmetry across a plane known as the twinned boundary.[24] The atomic arrangement on one side of the boundary is a mirror image of that on the other side. The twinned structure could stabilize the (100) facet in five-fold twinned nanowire structure even though the (100) facet is thermodynamically less stable compared to other facets like (111) with lower surface energy.[25,26] There have been relatively few reports of using t-CuNWs as CO_2RR catalysts, and they focus on low current density application in H-cells.[27–30] For example, Li *et al.* fabricated t-CuNWs with a diameter of approximately 20 nm to conduct CO_2RR in an H-cell with 0.1 M $KHCO_3$.[27] The t-CuNWs exhibited a high selectivity for CH_4 during CO_2RR, achieving a FE of 55% at -1.25 V *vs.* RHE ($\sim$15 mA cm^{-2}), although prolonged studies did lead to enhanced C_2H_4 production which was proposed to be due to morphology changes. Zhang *et al.* also synthesized t-CuNWs with diameter of both 25 nm and 50 nm to conduct CORR in an H-cell with 0.1 M $KHCO_3$.[28] The results indicated that the 50 nm t-CuNWs exhibit roughly two times higher C_2H_4 activity ($\sim$4 A g^{-1}) than that of 25 nm t-CuNWs ($\sim$2 A g^{-1}) under -1.1 V *vs.* RHE with a total current density of 10 mA cm^{-2}. Although the detailed reason was not discussed, it is possible that the abundance of (100) surface with larger diameter facilitated C–C coupling and induced more C_2H_4 production. Choi *et al.* also fabricated 25 nm t-CuNWs and conducted CO_2RR in an H-cell with 0.1 M $KHCO_3$,[29] producing C_2H_4 (C_2H_4 partial current density of $\sim$15 mA cm^{-2}) with low levels of CH_4 (CH_4 partial current density of $<$3 mA cm^{-2}) under -1.0 V *versus* RHE. In the case of Choi *et al.*, the C_2H_4 activity was linked to the *in situ* activation of the Cu

structure through the form of stable surface step sites where C–C coupling could occur. The current state-of-the-art CO_2RR results of t-CuNWs is summarized in Table S1, and it is apparent that the application of t-CuNWs working under high current density with membrane electrode assembly (MEA) is not previously studied, but that due to the presence of well-defined defect sites and the presence of (100) surface, t-CuNWs offer a potentially selective, stable catalyst for C_2 production.

To investigate the advantages of t-CuNWs, this study exploited (100)-enclosed t-CuNWs as catalysts for CO_2RR in a zero-gap configuration with 1 M KOH (unless otherwise specified) as the anolyte and a Ni fiber anode for water oxidation. The results showed that the (100)-enclosed t-CuNWs can sustain a high FE for C_2H_4 production at high current densities (100 mA cm^{-2}) with lower overpotential, highlighting their potential for practical CO_2RR applications. We also showed that the t-CuNWs possess higher hydrophobicity than CuNPs, supported by multiple measurements including electrode contact angle, outlet gas pressure, and oxygen reduction reaction (ORR) limiting current. The results not only demonstrate the superior activity and stability of t-CuNWs, but also provide valuable insights into the role of facet engineering and hydrophobicity in optimizing CO_2RR performance. By addressing key challenges in CO_2RR, this work demonstrates the potential of twinned structures with boundary defects as next-generation Cu catalysts for sustainable CO_2 utilization.

Results and discussion

Structural characterization of CuNPs and t-CuNWs

The scanning electron microscopy (SEM) and transmission electron microscopy (TEM) images of CuNPs in Fig. 1(a) and (b) showed that the diameter of CuNPs were approximately 40–50 nm. Notably, the exposed crystal facets include (111), (100), and (110), suggesting that the product distribution during CO_2RR may be wide.[12] Fig. 1(c) and (d) shows the SEM and TEM images of t-CuNWs, exhibiting a similar diameter of approximate 40–50 nm (detailed diameter distribution could be found in Fig. S1 in SI). In contrast to the CuNPs, the predominantly exposed facet of t-CuNW is {100}, as determined by the measured *d*-spacing in the enlarged image in Fig. 1(d) viewing from $\langle 100 \rangle$ direction. Note that multiple parallel line features could be observed in Fig. 1(d), while the twinned structure could not be resolved due to the $\langle 100 \rangle$ viewing direction, because the non-zero dot product between the $\langle 100 \rangle$ direction and the {111} plane normal, resulting in limited visibility of the corresponding lattice fringes of {111} twin boundary plane. To prove the existence of twinned structure, another t-CuNW with $\langle 110 \rangle$ viewing direction was chosen as shown in Fig. 1(e). The presence of twin boundaries within the t-CuNWs is confirmed by the split spots in fast Fourier transform (FFT) image (shown in the inset) from the marked region in Fig. 1(e), and inverse fast Fourier transform (IFFT) in Fig. 1(f) from the FFT in Fig. 1(e).

X-ray diffraction (XRD) results further supported the successful synthesis of t-CuNWs as shown in Fig. 1(g). The standard diffraction peaks of Cu at 2θ value are 43.2°, 50.4° and 74.8°, corresponding to (111), (200) and (220) planes,
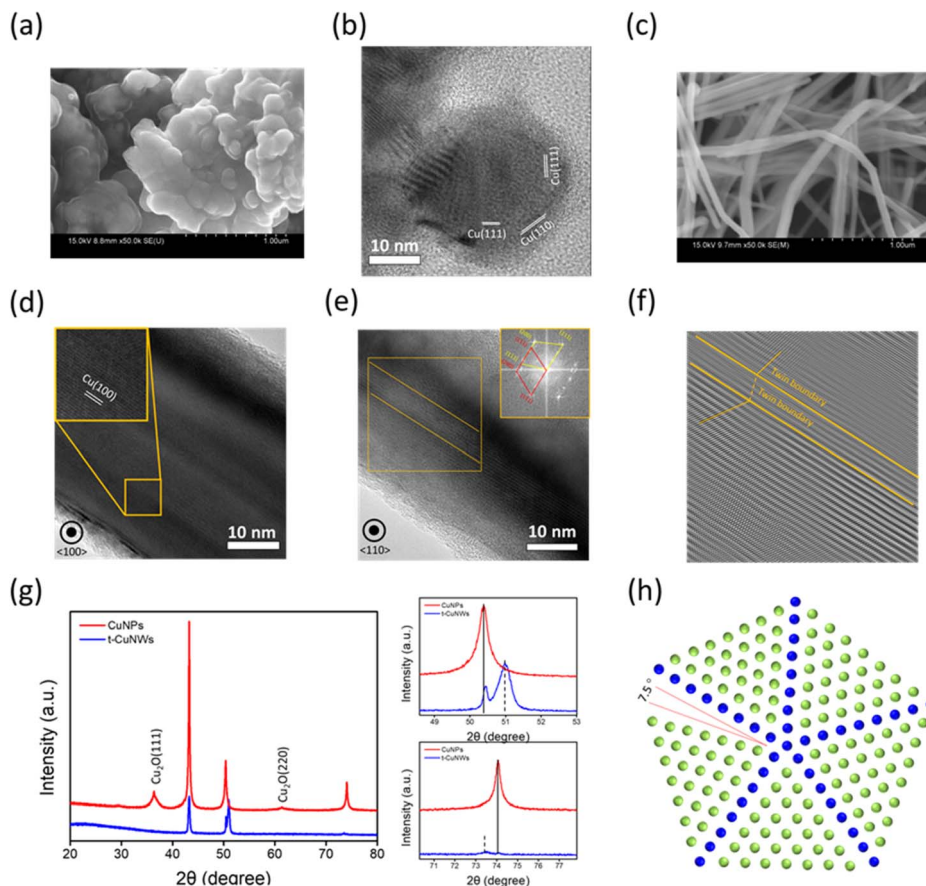
Fig. 1 (a) SEM image of commercial CuNPs; (b) TEM image of commercial CuNP showing multiple exposed facets; (c) SEM image of t-CuNWs; (d) TEM image of t-CuNW with {100} exposed facet viewing from ⟨100⟩ direction; (e) TEM image of t-CuNW showing twin boundaries viewing from ⟨110⟩ direction. The split diffraction spots in the inset are the FFT from the t-CuNW in (e), confirming the existence of twinned structure; (f) IFFT of the inset in (e), verifying the existence of twin boundaries; (g) XRD pattern of commercial CuNPs and fabricated t-CuNWs; (h) schematic image of the rotation degree in matrix and twin crystal.

respectively. Both CuNPs and t-CuNWs possessed all these diffraction peaks. There were two interesting phenomena observed in the XRD results. Firstly, the CuNPs possess Cu_2O diffraction peaks centered at 36.4° and 61.4°, corresponding to (111) and (220) facet, respectively. However, these Cu_2O peaks are absent in t-CuNWs. We also stored the t-CuNWs under ambient conditions for 60 days and remeasured the XRD as shown in Fig. S2. No obvious oxidation peaks were detected, indicating that the t-CuNWs fabricated with oleylamine was resistant to oxidation, possibly due to the protection of residue oleylamine on t-CuNWs surface, or that t-CuNWs structure is intrinsically more stable.[31–33] To further probe the surface composition of CuNPs and t-CuNWs, XPS was conducted to analyze the surface oxide (the detailed fitting method could be found in SI Note 1). The results in Fig. S3 showed that the ratio of Cu, Cu_2O and CuO were roughly 45%, 22% and 33% for CuNPs, while those for t-CuNWs (stored under ambient conditions for >60 days) were 67%, 21% and 12%, respectively. Although a minor amount of oxides were present on the surface of t-CuNWs, the lower amount of oxide indicated that t-CuNWs were more resistant to oxidation under ambient environment. We note that the lack of a charging effect in SEM (Fig. 1(c))

indicates that if present only a very thin layer of oleylamine was present on the outer surface of t-CuNW. Furthermore, ATR-FTIR was also conducted to analyze the existence of oleylamine residue on t-CuNWs surface as shown in Fig. S4. The t-CuNWs sample that had been washed did not show any evidence of the oleylamine ν(C–H) modes (2850, 2918 and 3319 cm^{-1}), indicating that the surface of t-CuNWs was clean without any detected oleylamine. XRD characterization of t-CuNWs that were only washed twice with hexane, and hence likely to retain the oleylamine was also recorded. In this case, the excess oleylamine formed a crystalline structure and possessed periodic peaks at lower degrees due to the long carbon chain inside polymer structure, which was observed as shown in Fig. S5.[34] The lack of the periodic peaks in the fully washed t-CuNW samples also supports our suggestion that if present the residual oleylamine is only present at low concentrations and any the stability is primarily due to the t-CuNW structure itself.

The XRD patterns of t-CuNWs also showed another (200) diffraction peak at 51.0°, and another (220) diffraction peak at 73.5°, indicating a large strain inside parts of the crystal. This distinctive peak split has been previously observed in both Ag and Cu nanowire systems.[35,36] It was suggested that these splits

served as an indicator of the five-fold twinned structure.[36] Typically, the twinned structure will rotate ~70.5° for each twin boundary as shown in Fig. 1(h). The t-CuNWs contained five twin boundaries, therefore five crystal domains would rotate ~352.5° around the axial direction. To match the gap for the remaining ~7.5°, compressive strain along (200) facet and tensile strain along (220) facet would be created in the center of the t-CuNWs to stabilize the structure, while shell region remain less strained, which induced the XRD peak split.[26,35] Similarly, the compressive strain along (200) facet increased the 2θ diffraction peak from 50.4° to 51.0° (enlarged image in Fig. 1(g)), while the tensile strain along (220) facet decreased the 2θ diffraction peak from 74.0° to 73.5° (enlarged image in Fig. 1(g)). Collectively, these structural analyses confirmed the successful fabrication of (100)-enclosed five-fold twinned CuNWs.

To confirm the exposed facets, both CuNPs and t-CuNWs were dropped on glassy carbon electrode with 1 mg cm^{-2} loading, and cyclic voltammetry (CV) was carried out in Ar-saturated 1 M KOH. Note that there are two regions to identify Cu facets. The peaks around +0.3 V to + 0.5 V belong to O-adsorption,[37–39] while the peaks around −0.2 V and +0.1 V belong to OH-adsorption.[40–43] Here, the CV was conducted using a potential range from −0.4 to 0.6 V vs. RHE with a scan rate of 50 mV s^{-1} to test the facet-dependent OH-adsorption. From Fig. 2, it is clear that the peaks around +0.3 V to +0.5 V are not obvious enough to identify the facets, and it is suggested that the electrochemical response around +0.3 V to +0.5 V is complicated by the incorporation of defect sites, which is substantially changed with the t-CuNW structure. Therefore, we utilized −0.2 V and +0.1 V to identify Cu(100) and Cu(111) rather than peaks around +0.3 V to +0.5 V. As shown in Fig. 2 and S6, no distinct OH-adsorption peak was observed across the scanned potential range for CuNPs, possibly due to the presence of a surface oxide layer that hindered direct OH-adsorption on the underlying copper facets. In contrast, the t-CuNWs catalyst exhibited an anodic peak around −0.2 V vs. RHE, which could

be associated with of OH-adsorption on the Cu(100) facet.[40–42] The absence of a noticeable peak near +0.1 V vs. RHE suggested minimal OH-adsorption on the Cu(111) facet.[40–42] The CV scans again highlighted that t-CuNWs might exhibit Cu(100) exposed facets.

Electrochemical measurement in a three-electrode system

First, we conducted measurements in a three-electrode (batch cell) system to understand the electrochemical behavior of commercial CuNPs and t-CuNWs, using 1 M KHCO$_3$ as electrolyte. In the linear sweep voltammetry (LSV) measurement shown in Fig. 3(a), the current density normalized by geometric area was higher for CuNPs in both Ar-saturated and CO$_2$-saturated electrolytes. However, considering the electrochemical surface area (ECSA) as measured by scan rate-dependent cyclic voltammetry and assuming the specific capacitance for Cu as 28 μF cm^{-2} (Fig. S7), the current normalized by ECSA is higher for t-CuNWs as shown in Fig. 3(b).[44] Two interesting phenomena could be drawn from the LSV measurements. Firstly, the current density for CuNPs and t-CuNWs were both lower in CO$_2$-saturated solution compared to Ar-saturated solution, suggesting the strong competition between the CO$_2$RR and HER. Secondly, the ECSA for t-CuNWs on GDE (220 μF cm^{-2}) was less than half of that for CuNPs on GDE (480 μF cm^{-2}), indicating that the hydrophobicity for t-CuNWs on GDE may be much higher than CuNPs on GDE. Therefore, the electrolyte cannot permeate to the inner catalyst layer for t-CuNWs on GDE, leading to a decreased ECSA.

To verify the enhanced hydrophobicity of t-CuNWs, contact angle measurements along with SEM images were conducted. The GDE used in this study (Sigracet 39BB) has a PTFE
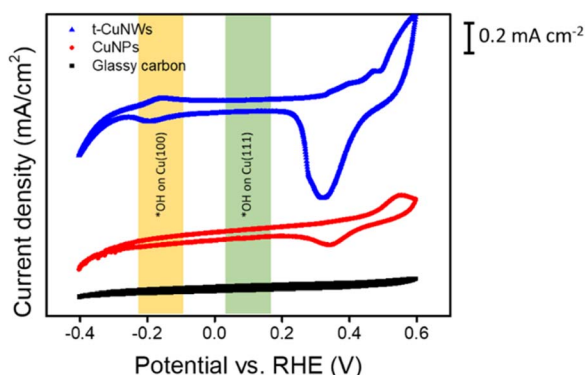

Fig. 2 Cyclic voltammetry of glassy carbon electrode, CuNPs and t-CuNWs in an Ar-saturated 1 M KOH from −0.4 to 0.6 V vs. RHE with a scan rate of 50 mV s^{-1}. Note that the cyclic voltammetry shown corresponded to the fifth cycle, which overlapped with the preceding four cycles as shown in Fig. S6, indicating stable electrochemical response.
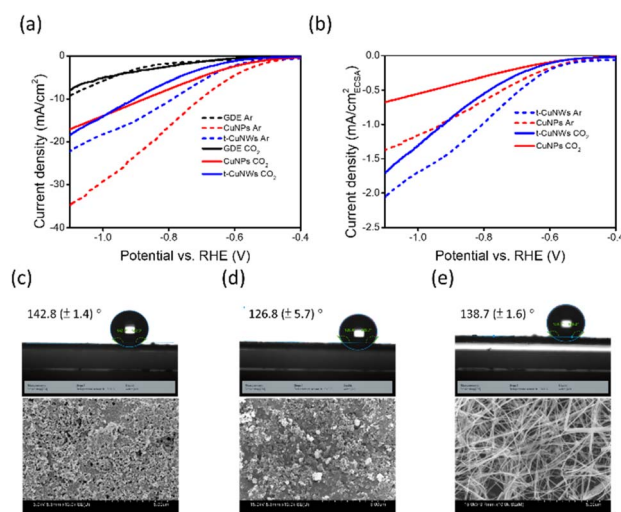

Fig. 3 (a) LSV curve normalized with geometric area of GDE, CuNPs and t-CuNWs in Ar-saturated and CO$_2$-saturated 1 M KHCO$_3$ solution in a three-electrode batch cell; (b) LSV curve normalized by ECSA of CuNPs and t-CuNWs in Ar-saturated and CO$_2$-saturated 1 M KHCO$_3$ solution. LSVs were performed at a scan rate of 50 mV s^{-1} from 0.1 V to −1.1 V vs. RHE; SEM images and contact angle measurements of (c) pure GDE (d) CuNPs on GDE (e) t-CuNWs on GDE with 1 M KHCO$_3$ droplet.

treatment to increase the hydrophobicity to reduce flooding. As shown in Fig. 3(c), the contact angle on a blank GDE was 142.8 ± 1.4°. After adding commercial CuNPs, the contact angle decreased to 126.8 ± 5.7°, in-line with the reported more hydrophilic nature of the Cu species.[45,46] Moreover, the slightly higher standard deviation (5.7°) could come from the randomly distributed CuNPs agglomerate as shown in the SEM image in Fig. 3(d) and EDX mapping in Fig. S8. As for t-CuNWs on GDE in Fig. 3(e), the contact angle was 138.7 ± 1.6°, which was similar to that of the blank GDE. It is proposed that the similar contact angle of t-CuNWs on GDE and pure GDE arises due to the entangled high aspect-ratio nanowire structure that created small pores in the middle, increased the capillary pressure, and therefore increased the hydrophobicity.[21] Similarly, the smaller standard deviation (1.6°) could also be due to the entangled nanowire structure that induced the homogenous t-CuNWs distribution on GDE. Note that we also conducted contact angle measurement with different solutions, including 1 M KOH and deionized water. All measurements showed the similar results that the contact angle followed the trend: blank GDE ≈ CuNWs on GDE > CuNPs on GDE as shown in Table S2.

CO₂RR performance in a zero-gap electrolyzer

The CO₂RR performance was conducted with a zero-gap electrolyzer with a water vapor-saturated CO₂ inlet at the cathode, and 1 M KOH anolyte, in a two-electrode system. A LSV scan was first conducted as shown in Fig. 4(a). It was clear that the t-CuNWs possess higher current density across the applied cell voltage. The anode structure is constant in all studies. Therefore, we propose that the higher current densities at smaller cell voltages is due to the cathode, either a result of decreased resistance, possibly due to better contact of the t-CuNWs with the AEM, or as a result of a change in the

electrocatalytic activity of the t-CuNWs. To decouple these two factors, electrochemical impedance spectroscopy (EIS) measurements were conducted, Fig. S9. The similar ohmic resistance from the EIS measurement indicates that the higher current density achieved by t-CuNWs in the electrolyzers assembly reflect higher intrinsic rates (lower overpotentials), concurring with the results in three-electrode system where the ECSA normalized current density for the t-CuNWs was higher when compared to the CuNPs. Note that the ECSA was 880 μF cm^{-2} for CuNPs and 690 μF cm^{-2} for t-CuNWs as shown in Fig. S10 and SI Note 2.

To obtain the product distribution as a function of applied current density, step chronopotentiometry was further conducted for both CuNPs and t-CuNWs as shown in Fig. 4(b). The t-CuNWs exhibited an overall lower cell voltage under the range of applied current density investigated here (up to 500 mA cm^{-2}). In addition to a significantly lower cell voltage ($\Delta V_{tNW/NP}$ = 150 mV at 100 mA cm^{-2}, 400 mV at 500 mA cm^{-2}) the product distributions were shown in Fig. 4(c) and (d) for CuNPs and t-CuNWs, respectively. At all of the applied current densities with CuNPs, the major product was H₂ (41–67% FE). At 100 mA cm^{-2}, the FE for CuNPs were 51 ± 2% (H₂), 13 ± 1% (CO), 5 ± 1% (CH₄) and 24 ± 2% (C₂H₄). In contrast for t-CuNWs with predominantly (100) exposed facets, at current densities <200 mA cm^{-2} selectivity towards the CO₂RR (vs. H₂ production) is achieved. At low current densities (25 mA cm^{-2}) on t-CuNW's CO is the primary product (54 ± 15% FE), as the current density is increased, C₂H₄ becomes the dominant product and at 100 mA cm^{-2}, the measured FEs were 30 ± 2% (H₂), 20 ± 7% (CO), and 41 ± 4% (C₂H₄), with negligible CH₄ being detected. We also quantified liquid products for t-CuNWs under 100 mA cm^{-2} by NMR, and detected HCOOH, C₂H₅OH, and C₃H₇OH at less than 1% FE as shown in Fig. S11. The reason that the C₂H₄ FE increased when the current was increased from 25 to 100 mA cm^{-2} could be attributed to a range of factors including (i) a higher local pH at the catalysts, which facilitated CO₂RR,[47–49] (ii) the higher local CO concentration at higher current density, enabling C–C coupling or (iii) an evolution of the t-CuNWs structure, with the *in situ* formation of step sites being previously proposed to lead to C₂ formation.[27,29]

To explore the impact of local CO/CO₂ concentration on the C₂ product selectivity, the effect of CO₂ inlet flow rate on the performance of the CuNPs and t-CuNWs was investigated by varying the flow rate from 80 to 40, 20, 10, and 5 sccm during studies at 100 mA cm^{-2}. As shown in Fig. S12(a) and (b), the H₂ FE gradually increased at low flow rates due to the depletion of CO₂ for both electrolyzers. Interestingly, the FE for C₂H₄ actually increased at higher flow rates for the t-CuNWs at 100 mA cm^{-2}. As the flow rate is increased (by a factor of ×16), CO produced that enters the gas phase is diluted but we do not see a drop in C₂H₄ product formation (which is formed by C–C coupling), suggesting that the dependence of the C₂H₄ FE on current density is not solely due to the local CO concentration changing.

To further investigate the current density dependent product selectivity of t-CuNWs in Fig. 4, chronopotentiometry was conducted firstly at 25 mA cm^{-2}, increased to 100 mA cm^{-2}, and
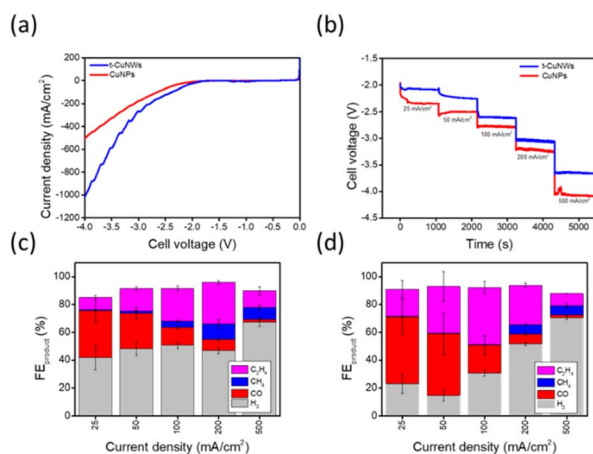

Fig. 4 (a) LSV scan of CuNPs and t-CuNWs in an AEM electrolyzer with a scan rate of 100 mV s^{-1} from 0 V to −4 V with a humidified CO₂ cathode feed (80 sccm) and a 1 M KOH anolyte; (b) step chronopotentiometry of CuNPs and t-CuNWs from 25 to 500 mA cm^{-2}; (c) product FE of CO₂RR for CuNPs; (d) product FE of CO₂RR for t-CuNWs. Error bars represent one standard deviation from at least three independent measurements.

then dropped back to 25 mA cm^{-2}. Past studies at low current densities in H-cells have correlated changes in product yield to an evolution of the t-CuNWs structure, with *in situ* formation of step sites being generated that enable C$_2$ formation.[29] In-line with these past reports here we find that after running at higher current density in the electrolyzer, when we switch back to 25 mA cm^{-2}, the FE for H$_2$ decreased, while the FE for CO greatly increased when compared to the same device operating with a pristine t-CuNW cathode, Fig. S13. Comparison TEM images before and after the Fig. S13 experiments were conducted as shown in Fig. S14. It was clear that the surface morphology of the t-CuNWs after 100 mA cm^{-2} was roughened compared to the as-synthesized t-CuNWs, which verified the reconstruction of surface structure under high current density that could change the product distribution,[27,29] but as is discussed below the twinned structure is retained.

Demonstration of the enhanced hydrophobicity for t-CuNWs in zero-gap cell

In addition to lower cell voltage and higher C$_2$H$_4$ FE for t-CuNWs, the long-term stability of the device, which is often related to hydrophobicity, should be another important factor that could affect the practical application in industries. To compare the hydrophobicity and extent of flooding of CuNPs and t-CuNWs on GDEs inside an AEM zero-gap electrolyzer, we measured the changes in gas pressure required to maintain a constant gas flow rate (see Fig. S15) whilst monitoring the CO$_2$RR products formed during electrolysis for two hours at 100 mA cm^{-2}, Fig. 5(a) and (b). We also measured (post-experiment after two hours of electrolysis) the volume of water that was condensed in a cold trap between the cathode gas outlet and the GC (see the schematic in Fig. S15), the contact angle for electrolyte on the Cu based GDEs, and also the pH (anolyte) change.

Our measurements indicate that the level of flooding (*i.e.* the extent of liquid penetration through the catalyst layer and the GDE) is greater for the CuNPs GDE compared to the t-CuNWs GDE. We propose that the cathode gas flow meter pressure reading (Fig. 6(a) and (b)) is a facile, *in situ*, measurement of the degree of flooding that does not require the electrolysis to be interrupted. Here we see a continuous pressure increase over the two hours of electrolysis only in CuNPs, which indicates that the porous electrode is becoming blocked, either by water or salt (carbonate) formation, which is known to occur readily in

AEM based CO$_2$RR electrolyzers, confirming the decreased flooding of the t-CuNWs cathode in more conventional post electrolysis measurements. Interestingly, the liquid volume that was trapped in the cold trap at the cathode outlet was also approximately three times higher for CuNPs (290 μL) compared to that of t-CuNWs (100 μL) as shown in Fig. S16, again supporting the conclusion that more water penetrates into and through the CuNPs GDE. The contact angle measurements with 1 M KOH after CO$_2$RR are summarized in Table S3. Although the contact angles for both CuNPs and t-CuNWs dropped significantly after the reaction, possibly due to the salt precipitation on the catalysts surface, resulting in the hydrophilic surface, the t-CuNWs still possessed higher contact angles, again in-line with the t-CuNWs decreasing flooding. The higher standard deviation for both CuNPs and t-CuNWs could come from the reason that some of the catalysts would stick to the AEM after electrolyzer disassembly, causing inhomogeneity on the surface.

To quantify the degree of flooding, we measured the gas transport resistance to the catalyst layer, using the oxygen reduction reaction (ORR) as a probe reaction. When the GDE was not flooded, the oxygen gas could reach the surface of the catalysts easily, inducing a higher ORR limiting current.[50,51] When the GDE floods, water fills the available gas channels, increasing the diffusion length of oxygen to the catalyst surface, decreasing the flux of oxygen to the catalyst surface and the ORR limiting current. The ORR was chosen because ORR occurs in a more positive potential than HER or CO$_2$RR, thus the limiting current is easily observed. To conduct ORR limiting current measurement, oxygen was mixed with argon in the concentration range of 0% to 2%, and LSVs were measured from 0 V to −3 V. As shown in Fig. S17, the ORR limiting current was taken to be at a cell voltage of −2 V because HER starts to onset, based on the 0% oxygen supply LSV curve. The summarized results were shown in Table S4, and it was obvious that the change of ORR limiting currents was minor for t-CuNWs after two hours CO$_2$RR compared to those of CuNPs. Fick's diffusion law was further introduced to get the effective diffusion length of oxygen to catalysts surface, and the calculated results were shown in Fig. 6(c) and (d) (SI Note 3 and Table S5). Based on this estimation, the diffusion length of oxygen for CuNPs changed from 21.4 to 26.0 nm (21.5% increase) as the schematic shown in Fig. 6(e), while that of t-CuNWs changed from 18.8 to 19.8 nm (5.4% increase) as the schematic shown in Fig. 6(f). In short, the enhanced hydrophobicity of t-CuNWs was verified through multiple methods, including gas pressure, the liquid volume, contact angle measurements and ORR limiting currents.

Post-electrolysis structural characterization of the CuNPs and t-CuNWs was also carried out. The XRD pattern of the CuNPs shows minimal changes (Fig. S18(a)). In contrast for t-CuNWs, the split peak of the t-CuNWs disappeared as shown in Fig. S18(b). This phenomenon suggests a relaxation of internal strain during CO$_2$RR, likely driven by electrochemical potential. Such behavior aligned with previous studies reporting that the applied electrochemical potential could induce strain, slightly rearrange atoms, and therefore modulate the internal strain, particularly in the highly strained t-CuNWs as
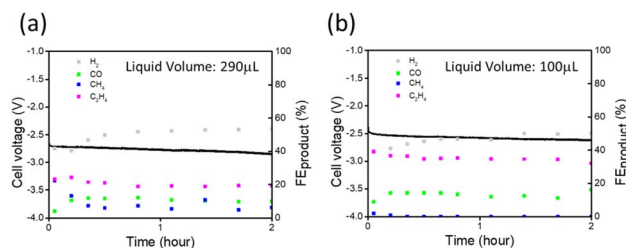

Fig. 5 CO$_2$RR two hours comparison of (a) CuNPs and (b) t-CuNWs running under 100 mA cm^{-2} 80 sccm CO$_2$ gas flow to cathode, 1 M KOH anolyte.
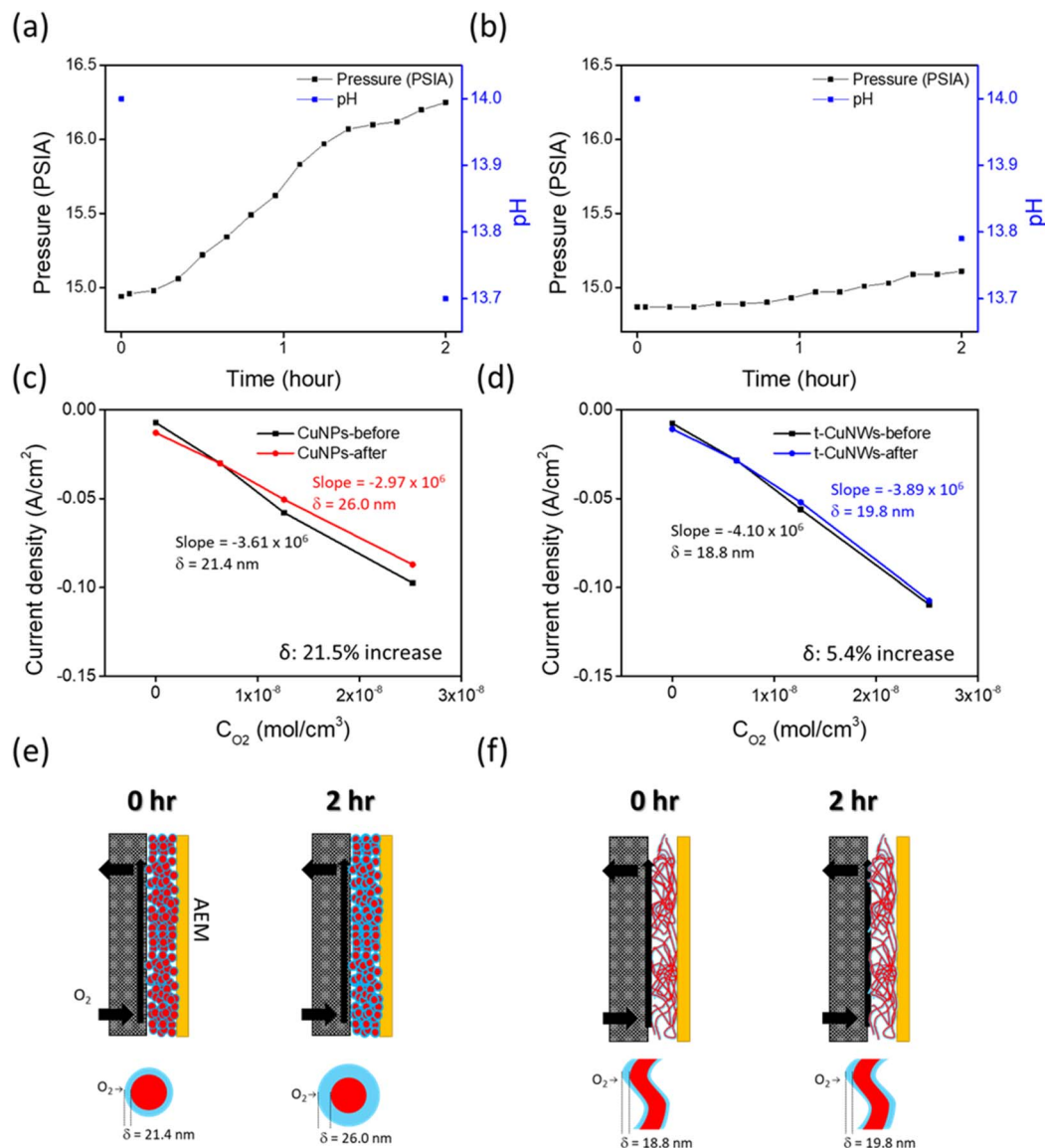
Fig. 6   Gas flow meter pressure and pH value measurement of (a) CuNPs and (b) t-CuNWs during CO_2RR at 100 mA cm^{-2} over a 2 hour period using a 80 sccm CO_2 gas flow to the cathode and 1 M KOH anolyte; calculated oxygen diffusion length for (c) CuNPs and (d) t-CuNWs before and after 2 hours CO_2RR; schematics of the calculated oxygen diffusion length for (e) CuNPs and (f) t-CuNWs.

the XRD shown in Fig. 1(g).[52,53] As for the morphology, both CuNPs and t-CuNWs showed little change based on the SEM results in Fig. S19. TEM results after prolonged electrolysis show some surface roughening, but importantly they confirm the twinned structure still existed, despite the strain being relieved, in t-CuNWs after two hours CO_2RR, based on the clear splitting diffraction spots and twin boundary as shown in Fig. S20.

Continuous CO_2RR and degradation analysis in a zero-gap cell

Initial experiments indicate that both Cu catalysts are stable but that water penetration (flooding) and potentially salt build up in the GDE may become limiting even on short runs. To test the limit of the zero-gap cell, continuous experiments until failure (the total blockage of gas channel) were conducted for

CuNPs and t-CuNWs as shown in Fig. S21(a) and (b), respectively. In-line with the data shown in Fig. 5, CuNPs GDEs showed a rapid decrease of C_2H_4 FE and a concomitant increase of HER, dropping to ~20% within 2 hours and then to ~10% by 3 hours. This was attributed to the water flooding at the catalyst layer, blocking CO_2 transport to the active sites for CO_2RR, as described above. Also supporting increased flooding in the CuNPs electrode, compared to the t-CuNWs electrodes was ECSA analysis (Fig. S22) that shows higher values for the CuNPs samples. The electrolyzer using the CuNPs completely stopped after operating for ~3.5 hours because the gas channel was completely blocked by salt precipitates as indicated by the sudden drop of voltage. The crossover of potassium ion from the anolyte to the cathode has been widely observed in AEM electrolyzers, and is widely considered as the

main reason for the decreased CO_2RR reaction (increased HER reaction).[18–20,54,55] Once the potassium ion crossed over to the cathode side, it would form bicarbonate or carbonate salts, which increased the rate of water flooding due to the hydrophilic character, and HER would dominate. After disassembling the electrolyzer, the precipitate could be clearly observed inside the gas channel in cathode plate and at the outlet gas line as shown in Fig. S23. SEM and EDX mapping were used to characterize the white precipitate as shown in Fig. S24. The SEM image showed the crystalline structure with sharp edges, and the EDX mapping confirmed the elements matching the species of K_2CO_3 or $KHCO_3$. XRD was further utilized and confirmed the diffraction peaks matching $KHCO_3$ as shown in Fig. S25.

For the long term performance of t-CuNWs, the C_2H_4 FE remained ~40% after operating for 4 hours. It was suggested that the higher C_2H_4 FE was attributed to the (100) exposed facet, and the higher electrode stability was due to the higher hydrophobicity although the gas line blockage still occurred soon after 4 hours operation, Fig. S21(b). The cell was

regenerated by disassembling the electrolyzer, rinsing away the white cathode salt in the gas channel and gas line, and reassembling the electrolyzer with all of the original components. The C_2H_4 production still remained ~40% FE as shown in Fig. S26, and TEM analysis after this prolonged repeated electrolysis also showed that the twinned structure still existed in t-CuNWs after CO_2RR based on the clear splitting diffraction spots and twin boundary as shown in Fig. S27. It is clear that the catalyst remains active and stable and that activity can be recovered once the electrode is dried and salt precipitates are removed.

Although the t-CuNW GDEs have significantly lower flooding/salt formation rates than CuNPs GDEs, it is clear that further improvements in electrode stability are required. In order to decrease salt formation and the associated flooding of the cathode GDE, we initially explored decreasing the anolyte concentration (which should lower K^+ crossover). However, in our device, this led to a rapid pH drop that ultimately decreased the CO_2RR activity (SI Note 4, 5, Fig. S28–33, and Table S6 for the detailed analysis). Instead, we found that periodic pauses
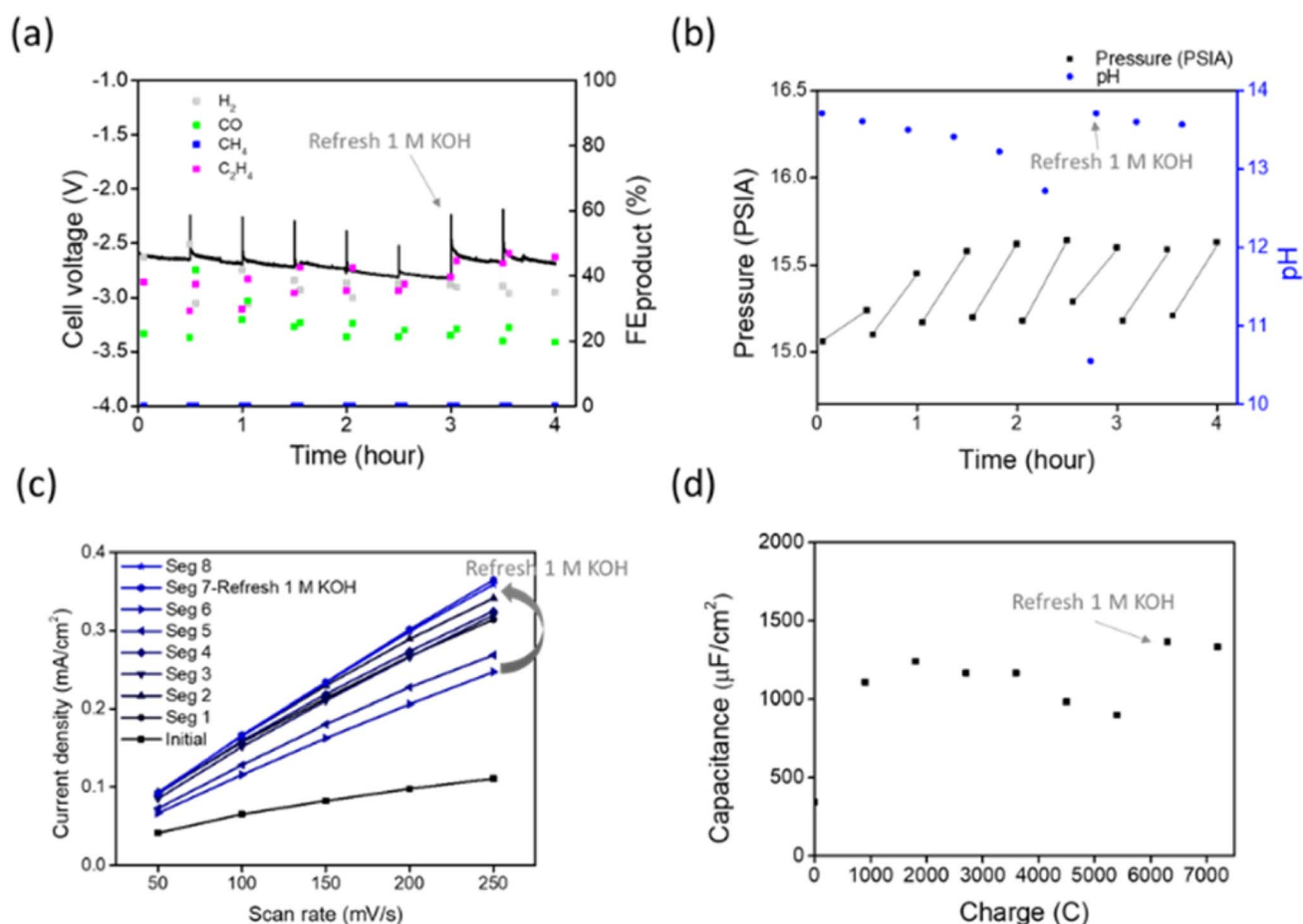

Fig. 7 (a) t-CuNWs CO_2RR segmented by ECSA measurement every 30 minute under 100 mA cm^{-2}, 80 sccm CO_2 gas flow, 1 M KOH anolyte; (b) gas flow meter pressure and pH value measurement; (c) current density vs. scan rate from 0 to −0.3 V cell voltage. (d) Double-layer capacitance from the slope of current density vs. scan rate in (c). Note that we refreshed the 100 mL 1 M KOH when the pH value approached 10 to prevent the anolyte damage the Ni anode. After refreshing, the cell voltage was restored to initial value and the activity increased, indicating the stability of the t-CuNWs cathode.

during electrolysis were an effective way to prevent flooding. Using ECSA as an indicator of the flooding,[56] it was found that periodic pauses (30 min of pause every 30 min of operation at 100 mA cm^{-2} during which an ECSA measurements is completed) led to a stable level of hydration in the t-CuNWs GDE as shown in Fig. 7. The product distribution is shown in Fig. 7(a), and detailed analysis of the gas pressure at the cathode (Fig. 7(b)) shows that the pressure increases during the 30 min chronopotentiometry periods due to the gradual flooding in the cathode. However, the gas pressure dropped during the pause in electrolysis when the ECSA measurement is carried out as the water/moisture is removed with the continuous CO_2 purging, which is also verified by the maintained capacitance value (Fig. 7(c) and (d)). The impact of drying the electrode periodically can be seen on the FE's of the products. The FE at the start of each electrolysis period (initial ~200 s of the 30 min) is higher for C_2H_4, than in the final (~1750 s of the 30 min) period, with FE being recovered again after the pause in electrolysis. The FE changes are proposed to be due to changes in water content in the GDE, based on our pressure measurement data. But we note that pulse electrolysis has been shown elsewhere to also restore activity through the creation of Cu_2O and subsequent reduction back to Cu.[57] Pulsed operation of the electrolyzer offers significant benefits but there is a trade-off between the increased electrode stability and the idle time of the device from the pulsing. Therefore, future work will investigate the optimal parameters for this innovative pulsed regeneration method.

Conclusions

The t-CuNWs was successfully synthesized with a facile and scalable oil bath heating method. The main products for CO_2RR using t-CuNWs in zero-gap electrolyzers with 1 M KOH feeding anolyte changed from CO to C_2H_4 as the applied current density (and cell voltage) increased. The higher selectivity of CO and C_2H_4 for t-CuNWs compared to that of commercial CuNPs was due to the abundance of (100) facets. In addition to the advantage of high CO and C_2H_4 selectivity, the nanowire structure endowed enhanced hydrophobicity to the electrode that increased the stability of the electrolyzer. Multiple supporting measurements, including gas pressure, collected liquid volume, contact angle, and ORR limiting current were utilized to demonstrate the enhanced hydrophobicity. A pulsed method during chronopotentiometry is proposed to increase the stability of the zero-gap electrolyzers. With the combination of facet engineering and morphology control, t-CuNWs were shown to be a promising candidate for industrial CO_2RR electrolyzers.

Experimental section

Materials

The following chemicals were used: KOH (≥85%, Sigma-Aldrich), $KHCO_3$ (≥99.5%, Sigma-Aldrich), isopropanol (99.5%, Sigma-Aldrich), absolute ethanol (Brenntag), carbon paper (Sigracet 39 BB, FuelCellStore), commercial Cu nanoparticles (99.5%, Sigma-Aldrich), H_2O (18.2 MΩ cm; deionized using Direct-Q® 3 UV water purification system; Merck), K_2SO_4 (≥99%, Sigma-Aldrich), $CuCl_2$ (99.999%, Sigma-Aldrich), D-(+)-glucose (≥99.5%, Sigma-Aldrich), oleylamine (70%, Sigma-Aldrich), hexane (99.999%, Sigma-Aldrich), 250 μm nickel fiber sheet (Currento® PTL Ni-60/250, Bekaert), Sustainion membrane (X37-50 Grade RT, FuelCellStore), 5 wt% Sustainion solution (XA-9, Dioxide Materials), bipolar membrane (Fumasep FBM), D_2O (99.9%, Sigma-Aldrich), DMSO (≥99.8%, Fluka), KBr (≥99.0%, Sigma-Aldrich).

Synthesis of five-fold twinned copper nanowires (t-CuNWs)

The synthesis of t-CuNWs was modified from literature.[27,28,30,32] Firstly, 135 mg of $CuCl_2$ and 135 mg of D-(+)-glucose were dissolved in 10 g of oleylamine under an ambient atmosphere. Then, the mixture was gradually heated from room temperature to 110 °C in 20 minutes with a stir bar rotating at 400 rpm, and continued for 2 hours until the solution turned brown, indicating the formation of oleyamine-coordinated Cu(II) solution. Subsequently, the temperature was increased to 160 °C in 20 minutes without stirring, and maintained for 8 hours to facilitate nanowire growth. The resulting t-CuNWs were isolated via centrifugation at 6000 rpm for 5 minutes and washed three times with hexane and once with a 1 : 1 (by volume) mixture of hexane and absolute ethanol to remove surface ligands and other unreacted precursors. Finally, the solvent was evaporated to collect t-CuNWs. The collected t-CuNWs were stored in closed vials until the subsequent hand spraying process on carbon paper. Note that the commercial CuNPs with 40–60 nm diameter were used as comparison.

Electrode fabrication

The t-CuNWs or CuNPs cathode was prepared by hand spraying an ink of dispersed t-CuNWs or CuNPs on carbon paper with the loading of 1 mg cm^{-2}. For the ink, 1 mg cm^{-2} of t-CuNWs or CuNPs and 1 μL cm^{-2} Sustainion solution was added into isopropanol (0.2 mL cm^{-2}). The ink was stirred for 1 hour before spraying. The ink was hand sprayed on a carbon paper held at a 60 °C hot plate with an airbrush of N_2. After spraying, the electrode was left under ambient conditions to dry before assembly.

Electrolyzer setup

Electrochemical measurements were conducted in an electrolyzer (Dioxide Materials, cathode plate (stainless steel) 5 cm^2, anode plate (titanium) 9 cm^2, serpentine flow channels with channel width of 0.7 mm) with an Ivium Vertex potentiostat. Cu, either commercial CuNPs or t-CuNWs, was utilized as cathode. Ni fiber was utilized as anode. Sustainion membrane was utilized as anion exchange membrane (AEM) in a zero-gap configuration. The membrane was initially immersed into 1 M KOH for 24 hours, washed with de-ionized water and then transferred to 1 M $KHCO_3$ for another 72 hours to fully convert the membrane into either carbonate or bicarbonate form. Before assembly, the membrane would be washed with de-ionized water for three times on each side.

The electrolyzer was assembled with nine screws with a fixed torque of 3 N m. The inlet CO_2 flow was set at 80 sccm controlled by a mass flow controller (Buerkert or Alicat) and was passed through a water bubbler at room temperature. The 1 M KOH anolyte was circulated with a peristaltic pump at 0.4 mL s^{-1}. All the experiments were conducted under ambient conditions (1 atm and 20–22 °C).

Electrochemical facet characterization and initial activity measurements were conducted in a three-electrode system with a Ag/AgCl reference electrode for 1 M KHCO$_3$ cell solution, and a Hg/HgO reference electrode for 1 M KOH cell solution. Pt wire was utilized as counter electrode. The catalysts were deposited on either a glassy carbon electrode (0.196 cm^2) or on the same carbon paper as the electrolyzer measurements.

To evaluate the ORR limiting current, a gas mixture of O$_2$ and Ar was pre-mixed at controlled flow rates before entering the zero-gap electrolyzer. Specifically, O$_2$ and Ar were combined at volumetric flow ratios of 0.5, 1, and 2% of O$_2$ balanced with Ar, while maintaining a constant total 100 sccm flow rate. The gas mixture was introduced into the electrolyzer to systematically vary the partial pressure of O$_2$ and thereby determine the diffusion-limited current under different O$_2$ concentrations. The method of calculation of oxygen diffusion length from the measured ORR current density could be found in SI Note 3.

Characterization

The diameter and length of CuNPs and t-CuNWs were determined through scanning electron microscopy (SEM, Hitachi S4800). The phase identification and crystallographic textures were characterized using X-ray diffraction (XRD, Rigaku Smartlab Thin Films) with copper source and transmission electron microscopy (TEM, JEM-2100+, JEOL) with 200 kV accelerating voltage. The hydrophobicity was analyzed through contact angle measurement using 1 M KHCO$_3$, 1 M KOH, and deionized water with a droplet size of 10 μL. The results were averaged with at least three measurements (DSA100 Expert Drop Shape Analyser). For liquid sample, Fourier-transform infrared (FTIR) spectroscopy (Thermo Fisher Scientific, Nicolet iS50 Spectrometer) was performed to characterize the species present in the aqueous solution. For solid samples, attenuated total reflection Fourier-transform infrared spectroscopy (ATR-FTIR, Bruker, TENSOR II) was utilized to analyze the oleylamine residue. Prior to measurement, the samples (t-CuNWs and oleylamine) were finely ground and thoroughly mixed with KBr. The mixture was then pressed into a transparent pellet under high pressure using a pellet die. The resulting KBr pellet was placed directly onto the ATR crystal, and spectra were recorded over a range of 4000–400 cm^{-1} with a resolution of 2 cm^{-1}. The surface chemical composition was analyzed through XPS (Thermo NEXSA) using monochromated Al Kα X-rays (1486.69 eV) at 6 mA emission and 12 kV HT (0 W), an elliptical spot size of 400 μm, and a 180° hemispherical analyser in conjunction with a two-dimensional detector that integrates intensity across the entire angular distribution range. The instrument was calibrated to gold metal Au 4f (83.95 eV) and dispersion adjusted give a BE of 932.6 eV for the Cu 2p$_{3/2}$ line of metallic copper. The

source resolution for monochromated Al Kα X-rays is ~0.3 eV. Charge compensation was achieved using a low energy electron flood gun, operating with a current of 6 mA, until the C 1s feature reported a symmetric Gaussian peak shape.

Conflicts of interest

There are no conflicts to declare.

Data availability

The data supporting this article have been included in part as part of the SI. See DOI: **https://doi.org/10.1039/d5se01129a**.

Acknowledgements

References

1 International Energy Agency, 2024, **https://www.iea.org/reports/co2-emissions-in-2023**.

2 C. P. O'Brien, R. K. Miao, A. Shayesteh Zeraati, G. Lee, E. H. Sargent and D. Sinton, *Chem. Rev.*, 2024, **124**, 3648–3693.

3 M. Jouny, W. Luc and F. Jiao, *Ind. Eng. Chem. Res.*, 2018, **57**, 2165–2177.

4 T. Moore, D. I. Oyarzun, W. Li, T. Y. Lin, M. Goldman, A. A. Wong, S. A. Jaffer, A. Sarkar, S. E. Baker, E. B. Duoss and C. Hahn, *Joule*, 2023, **7**, 782–796.

5 Y. Li, Y. Sun and M. Yu, *Adv. Funct. Mater.*, 2024, **34**, 2410186.

6 F. Wang, Z. Lu, H. Guo, G. Hao, W. Jiang and G. Liu, *Coord. Chem. Rev.*, 2024, **515**, 215962.

7 N. Zhang and Y. Zhang, *Appl. Catal., B*, 2025, **363**, 124822.

8 H. Zhang, C. He, S. Han, Z. Du, L. Wang, Q. Yun, W. Cao, B. Zhang, Y.-H. Tian and Q. Lu, *Chin. Chem. Lett.*, 2022, **33**, 3641–3649.

9 G. Zhang, Z.-J. Zhao, D. Cheng, H. Li, J. Yu, Q. Wang, H. Gao, J. Guo, H. Wang, G. A. Ozin, T. Wang and J. Gong, *Nat. Commun.*, 2021, **12**, 5745.

10 Y. Hori, I. Takahashi, O. Koga and N. Hoshi, *J. Phys. Chem. B*, 2002, **106**, 15–17.

11 Y. Hori, I. Takahashi, O. Koga and N. Hoshi, *J. Mol. Catal. A: Chem.*, 2003, **199**, 39–47.

12 G. L. De Gregorio, T. Burdyny, A. Loiudice, P. Iyengar, W. A. Smith and R. Buonsanti, *ACS Catal.*, 2020, **10**, 4854–4862.

13 Y. Xu and L. Zhang, *Catalysts*, 2024, **14**, 468.

14 D. Cheng, K.-L. C. Nguyen, V. Sumaria, Z. Wei, Z. Zhang, W. Gee, Y. Li, C. G. Morales-Guio, M. Heyde, B. Roldan

Cuenya, A. N. Alexandrova and P. Sautet, *Nat. Commun.*, 2025, **16**, 4064.

15 Y. Yang, S. Louisia, S. Yu, J. Jin, I. Roh, C. Chen, M. V. Fonseca Guzman, J. Feijóo, P.-C. Chen, H. Wang, C. J. Pollock, X. Huang, Y.-T. Shao, C. Wang, D. A. Muller, H. D. Abruña and P. Yang, *Nature*, 2023, **614**, 262–269.

16 Y. Yang, C. Shi, J. Feijóo, J. Jin, C. Chen, Y. Han and P. Yang, *J. Am. Chem. Soc.*, 2024, **146**, 23398–23405.

17 J. Vavra, T. H. Shen, D. Stoian, V. Tileli and R. Buonsanti, *Angew. Chem.*, 2021, **133**, 1367–1374.

18 B. Ó. Joensen, J. A. Zamora Zeledón, L. Trotochaud, A. Sartori, M. Mirolo, A. B. Moss, S. Garg, I. Chorkendorff, J. Drnec, B. Seger and Q. Xu, *Joule*, 2024, **8**, 1754–1771.

19 H. Simonson, D. Henckel, W. E. Klein, K. C. Neyerlin and W. A. Smith, *ACS Sustainable Chem. Eng.*, 2025, **13**, 823–833.

20 Y. Kong, H. Hu, M. Liu, Y. Hou, V. Kolivoška, S. Vesztergom and P. Broekmann, *J. Catal.*, 2022, **408**, 1–8.

21 S. Chen, B. Rowley, R. Ganganahalli and B. S. Yeo, *Adv. Sci.*, 2024, **11**, 2405938.

22 N. T. Nesbitt, T. Burdyny, H. Simonson, D. Salvatore, D. Bohra, R. Kas and W. A. Smith, *ACS Catal.*, 2020, **10**, 14093–14106.

23 A. Conte, M. Baron, S. Bonacchi, S. Antonello and A. Aliprandi, *Nanoscale*, 2023, **15**, 3693–3703.

24 T. Hahn and H. Klapper, in *International Tables for Crystallography Volume D: Physical Properties of Crystals*, ed. A. Authier, Springer Netherlands, Dordrecht, 2003, pp. 393–448.

25 J. Wu, T. Sun and X. Tang, *Scr. Mater.*, 2024, **240**, 115860.

26 X. Qi, Z. Chen, T. Yan and K. A. Fichthorn, *ACS Nano*, 2019, **13**, 4647–4656.

27 Y. Li, F. Cui, M. B. Ross, D. Kim, Y. Sun and P. Yang, *Nano Lett.*, 2017, **17**, 1312–1317.

28 H. Zhang, Y. Zhang, Y. Li, S. Ahn, G. T. R. Palmore, J. Fu, A. A. Peterson and S. Sun, *Nanoscale*, 2019, **11**, 12075–12079.

29 C. Choi, S. Kwon, T. Cheng, M. Xu, P. Tieu, C. Lee, J. Cai, H. M. Lee, X. Pan, X. Duan, W. A. Goddard and Y. Huang, *Nat. Catal.*, 2020, **3**, 804–812.

30 Z. Lyu, S. Zhu, M. Xie, Y. Zhang, Z. Chen, R. Chen, M. Tian, M. Chi, M. Shao and Y. Xia, *Angew. Chem., Int. Ed.*, 2021, **60**, 1909–1915.

31 Z. B. Wang, K. Lu, G. Wilde and S. V. Divinski, *Acta Mater.*, 2010, **58**, 2376–2386.

32 T. Zhang, W.-Y. Hsieh, F. Daneshvar, C. Liu, S.-P. Rwei and H.-J. Sue, *Nanoscale*, 2020, **12**, 17437–17449.

33 H.-Y. Chen, H.-Y. T. Chen and C.-N. Liao, *Appl. Surf. Sci.*, 2025, **692**, 162753.

34 A. Loubat, L.-M. Lacroix, A. Robert, M. Impéror-Clerc, R. Poteau, L. Maron, R. Arenal, B. Pansu and G. Viau, *J. Phys. Chem. C*, 2015, **119**, 4422–4430.

35 Y. Sun, Y. Ren, Y. Liu, J. Wen, J. S. Okasinski and D. J. Miller, *Nat. Commun.*, 2012, **3**, 971.

36 H.-J. Yang, S.-Y. He and H.-Y. Tuan, *Langmuir*, 2014, **30**, 602–610.

37 L. Cao, D. Raciti, C. Li, K. J. T. Livi, P. F. Rottmann, K. J. Hemker, T. Mueller and C. Wang, *ACS Catal.*, 2017, **7**, 8578–8587.

38 Z. Chen, Z. Ma, G. Fan and F. Li, *ACS Appl. Mater. Interfaces*, 2024, **16**, 35143–35154.

39 Z. Xie, Q. Wang, H. Yang, J. Feng, J. Chen, S. Song, C. Meng, K. Wang and Y. Tong, *Small*, 2024, **20**, 2401530.

40 K. J. P. Schouten, E. P. Gallent and M. T. M. Koper, *J. Electroanal. Chem.*, 2013, **699**, 6–9.

41 A. K. Engstfeld, T. Maagaard, S. Horch, I. Chorkendorff and I. E. L. Stephens, *Chem.–Eur. J.*, 2018, **24**, 17743–17755.

42 A. Tiwari, H. H. Heenen, A. S. Bjørnlund, T. Maagaard, E. Cho, I. Chorkendorff, H. H. Kristoffersen, K. Chan and S. Horch, *J. Phys. Chem. Lett.*, 2020, **11**, 1450–1455.

43 S. J. Raaijman, N. Arulmozhi, A. H. M. da Silva and M. T. M. Koper, *J. Electrochem. Soc.*, 2021, **168**, 096510.

44 J. Pan, Y. Sun, P. Deng, F. Yang, S. Chen, Q. Zhou, H. S. Park, H. Liu and B. Yu Xia, *Appl. Catal., B*, 2019, **255**, 117736.

45 Z. Xing, L. Hu, D. S. Ripatti, X. Hu and X. Feng, *Nat. Commun.*, 2021, **12**, 136.

46 S. Feng, Y. Xing, S. Deng, W. Shang, D. Li, M. Zhang, Y. Hou and Y. Zheng, *Adv. Mater. Interfaces*, 2018, **5**, 1701193.

47 J. Li, Z. Wang, C. McCallum, Y. Xu, F. Li, Y. Wang, C. M. Gabardo, C.-T. Dinh, T.-T. Zhuang, L. Wang, J. Y. Howe, Y. Ren, E. H. Sargent and D. Sinton, *Nat. Catal.*, 2019, **2**, 1124–1131.

48 M. Schreier, Y. Yoon, M. N. Jackson and Y. Surendranath, *Angew. Chem.*, 2018, **57**, 10221–10225.

49 J. Li, K. Chang, H. Zhang, M. He, W. A. Goddard III, J. G. Chen, M.-J. Cheng and Q. Lu, *ACS Catal.*, 2019, **9**, 4709–4718.

50 Y. V. Yakovlev, M. G. Rodríguez, Y. V. Lobko, M. Vorokhta, P. Kúš, I. Matolínová and V. Matolín, *Electrochim. Acta*, 2022, **404**, 139755.

51 S. Wang, Y. n. Liang, D. Li, Z. Zhang and J. Zhang, *Int. J. Hydrogen Energy*, 2022, **47**, 23762–23771.

52 A. Hrnjic, A. R. Kamšek, A. Pavlišič, M. Šala, M. Bele, L. Moriau, M. Gatalo, F. Ruiz-Zepeda, P. Jovanovič and N. Hodnik, *Electrochim. Acta*, 2021, **388**, 138513.

53 C. Atlan, C. Chatelier, I. Martens, M. Dupraz, A. Viola, N. Li, L. Gao, S. J. Leake, T. U. Schülli, J. Eymery, F. Maillard and M.-I. Richard, *Nat. Mater.*, 2023, **22**, 754–761.

54 Z. Liu, H. Yang, R. Kutz and R. I. Masel, *J. Electrochem. Soc.*, 2018, **165**, J3371.

55 T. Bi, R. Xue, Y. Jiang, S. Yuan, C. Zhao, G. Zhang, X. Cheng, J. Yin, G. Wei, X. Yan and J. Zhang, *Int. J. Hydrogen Energy*, 2024, **90**, 784–791.

56 M. E. Leonard, L. E. Clarke, A. Forner-Cuenca, S. M. Brown and F. R. Brushett, *ChemSusChem*, 2020, **13**, 400–411.

57 N. B. D. Monti, G. A. El-Nagar, M. Fontana, F. Di Costola, S. Gupta, M. T. Mayer, C. F. Pirri and J. Zeng, *Mater. Today Sustain.*, 2025, **30**, 101124.